


FULL PAPER

Open Access



Thermospheric wind response to a sudden ionospheric variation in the trough: event at a pseudo-breakup during geomagnetically quiet conditions

Shin-ichiro Oyama^{1,2,3*} , Heikki Vanhamäki³, Lei Cai³, Anita Aikio³, Michael Rietveld⁴, Yasunobu Ogawa⁵, Tero Raita⁶, Mirjam Kellinsalmi⁷, Kirsti Kauristie⁷, Boris Kozelov⁸, Atsuki Shinbori¹, Kazuo Shiokawa¹, Takuo T. Tsuda⁹ and Takeshi Sakanoi¹⁰

Abstract

The thermospheric wind response to a sudden westward turning of the ion velocity at a high latitude was studied by analyzing data obtained with a Fabry–Perot interferometer (FPI; 630 nm), Dynasonde, and Swarm A & C satellites during a conjunction event. The event occurred during a geomagnetically quiet period ($K_p = 0+$) through the night, but some auroral activity occurred in the north. The collocated FPI and Dynasonde measured the thermospheric wind (\mathbf{U}) and ionospheric plasma velocity (\mathbf{V}), respectively, in the F region at the equatorward trough edge. A notable scientific message from this study is the possible role of thermospheric wind in the energy dissipation process at F-region altitude. The FPI thermospheric wind did not instantly follow a sudden \mathbf{V} change due to thermospheric inertia in the F region. At a pseudo-breakup during the event, \mathbf{V} suddenly changed direction from eastward to westward within 10 min. \mathbf{U} was concurrently accelerated westward, but its development was more gradual than that of \mathbf{V} , with \mathbf{U} remaining eastward for a while after the pseudo-breakup. The delay of \mathbf{U} is attributed to the thermospheric inertia. During this transition interval, $\mathbf{U} \cdot \mathbf{V}$ was negative, which would result in more efficient generation of frictional heating than the positive $\mathbf{U} \cdot \mathbf{V}$ case. The sign of $\mathbf{U} \cdot \mathbf{V}$, which is related to the relative directions of the neutral wind and plasma drift, is important because of its direct impact on ion-neutral energy exchange during collisions. This becomes especially important during substorm events, where rapid plasma velocity changes are common. The sign of $\mathbf{U} \cdot \mathbf{V}$ may be used as an indicator to find the times and locations where thermospheric inertia plays a role in the energy dissipation process.

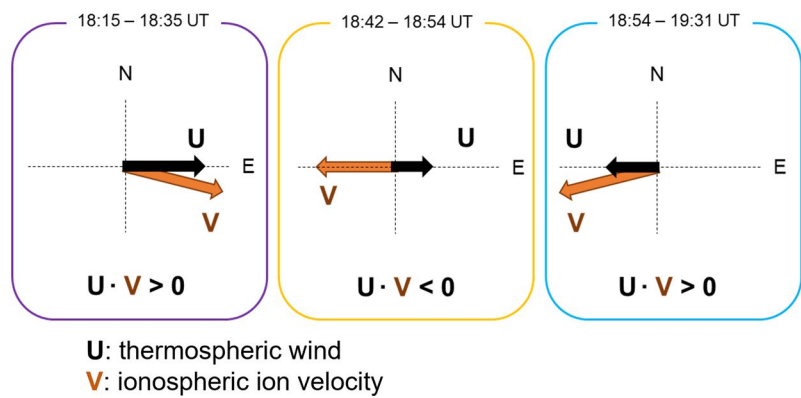
Keywords: Ionosphere, Thermosphere, Ion drag, High latitude, Fabry–Perot interferometer, Aurora, Pseudo-breakup

*Correspondence: soyama@isee.nagoya-u.ac.jp

¹ Institute for Space-Earth Environmental Research, Nagoya University, Nagoya, Japan

Full list of author information is available at the end of the article

Graphical Abstract



Introduction

To understand the dynamics of the auroral thermosphere at F-region altitudes in the dusk sector, the momentum balance in the zonal components of the ionospheric plasma flow and thermospheric neutral wind is a decisive factor. The westward flow is predominant in the ionospheric convection at the dusk side but the global-scale pressure gradient between the day and night hemispheres in the thermospheric wind field acts as a background forcing, which tends to push the air eastward. Ion drag likely overcomes the pressure gradient through the particle collisional process, particularly during periods of geomagnetic disturbance (Killeen et al. 1984; Sakanoi et al. 2002). The relative speed between the ionospheric and thermospheric flows generates frictional heating, which results in equatorward thermospheric winds from the auroral latitudes to the lower latitudes. The equatorward flow is rotated westward by the Coriolis force, in the same direction as the ion drag in the dusk sector. Therefore, westward turning of the thermospheric wind at F-region altitudes is often observed in the dusk sector along with commencement of the geomagnetically active period (Conde et al. 2001; Cai et al. 2019). At the equatorward side of the auroral oval or outside of the ionospheric convection, the thermospheric wind may still flow eastward due to weaker contributions of the ion drag (Dhadly and Conde 2017). However, the eastward thermospheric wind can be overturned by a fast plasma flow, such as the subauroral polarization stream (SAPS), which may appear in the ionospheric trough (e.g., Foster and Burke 2002).

The ionospheric trough appears in a meridionally narrow but zonally elongated region at the equatorward

side of the auroral oval, particularly near the dusk solar terminator. The latitude tends to shift equatorward, synchronizing with expansion of the auroral oval or geomagnetic activity. Various conspicuous features have been observed in the ionospheric trough with optical and radio wave techniques. The SAPS is a notable feature which appears in the ionospheric trough, and was found in ionospheric radar measurements with characteristics of westward or sunward high-speed plasma flows in the F region in the dusk sector (Foster and Vo 2002; Koustov et al. 2008; Kataoka et al. 2009; Nagano et al. 2015). The perpendicular electric field to drive the westward plasma flow is directed poleward. This is consistent with the direction of the ionospheric closure current, which connects the Region 2 (R2) downward field-aligned current (FAC) to the R1 upward FAC across the ionospheric trough. The generation mechanism of the poleward electric field is still under debate between the voltage generator mechanism (Southwood and Wolf 1978; De Keyser et al. 1998) and the current generator mechanism (Karlsson et al. 1998; Anderson et al. 2001). Before reports of the SAPS from radar measurements, the poleward electric field was found in satellite measurements (Smiddy et al. 1977; Maynard 1978; Spiro et al. 1979; Rich et al. 1980). Later improvement of the sensor sensitivity enabled measurements of the fine structure in the latitudinal pattern of the electric field (Erickson et al. 2016; Horvath and Lovell 2017). Horvath and Lovell (2017) found double-peak subauroral ion drift (DSAID) in measurements performed with the Defense Meteorological Satellite Program (DMSP) when it flew across the ionospheric trough at an approximately 840-km altitude. They

suggested that the associated double-layer R2 FACs could be the main driver. Fine structures of the subauroral electric field have also been found with ground-based radars (Makarevich and Bristow 2014).

It is conceivable that high-speed westward ion flows in the SAPS region can accelerate the thermosphere westward by particle collisions. Wang et al. (2011, 2012a, b) performed a statistical analysis of measurements from DMSP and the Challenging Minisatellite Payload (CHAMP) to study the thermospheric wind response to the SAPS. The dataset was grouped into two geomagnetic activity levels, higher and lower than K_p of 4. The westward wind peaked at approximately the same latitude as the SAPS did for both geomagnetic activity levels but the wind magnitude in summer was larger than that in winter, which is an opposite tendency to the SAPS seasonal dependence. Evolution of the thermospheric response to storm-time energy dissipations at high latitudes suggests that thermospheric dynamics interrelate with various events that are widely distributed longitudinally and latitudinally. To reveal the thermospheric responses to the SAPS, it might be best to analyze measurements during periods of moderately quiet conditions, but with some auroral activity, when it may be possible to distinguish thermospheric variations according to their mechanisms by minimizing external effects of, for instance, heating and ion drag from the high-latitude plasma convection.

This study analyzes the thermospheric and ionospheric velocities during a period of geomagnetically quiet conditions with K_p value of 0+ but including a pseudo-breakup on 20 February 2018. In general, it would be acceptable to assume that K_p of 0+ is a level of the quiet condition. It is, however, likely that K_p index overlooks events occurring at relatively high latitudes. Measurements were made with a Fabry–Perot interferometer (FPI; wavelength of 630.0 nm) and the Dynasonde, which are collocated at the Tromsø European Incoherent Scatter (EISCAT) radar site (geographic coordinates 69.58°N, 19.22°E). The FPI and Dynasonde measurements were performed in the ionospheric trough that was identified with the Swarm satellites. An ephemeral red arc was found at the ionospheric trough minimum, coinciding with pseudo-breakup (Oyama et al. 2020). This study focuses on the responses of the thermospheric wind (U) to a sudden westward turning of the ionospheric plasma velocity (V) at pseudo-breakup in the F region. There are many reports on thermospheric wind variations at high latitudes, but this study focuses on evaluation of $U \cdot V$ in the F region to examine the role of thermospheric wind in the energy dissipation process at a sudden change in the ionospheric ion velocity. This study has successfully retrieved the thermospheric wind role by analyzing geomagnetically quiet-time data with a pseudo-breakup.

Previous works for thermospheric wind effects on the Joule heating rate have been made mainly on the E-region events (Lu et al. 1995; Thayer, 1998), although some studies suggest an important issue on thermospheric wind contributions to energy dissipation in the F region based on simulation (Billett et al. 2018; Eyiguler et al. 2018) and observations (Oyama et al. 2009; Kiene et al. 2019; Billett et al. 2020). The sign of $U \cdot V$ was calculated in an ion-neutral coupling study (Kiene et al. 2019) and applied to evaluation of the thermospheric wind contributions. While larger negative $U \cdot V$ should decrease the Joule heating rate if things go according to a theoretical prediction, there are notable number of exceptions in measurements. F-region $U \cdot V$ and its role on the energy dissipation process should be investigated more.

Measurements and the background

Fabry–Perot interferometer

The FPI has been operated since January 2009 at the Tromsø EISCAT radar site for winter months (mainly from the middle of September to the beginning of April). The FPI mounts a filter wheel and a sky scanner allowing for sequential measurements by selecting one of the optical filters (channels 1–3: 557.7, 630.0, and 732.0 nm, respectively) and directions of the line of sight (any azimuth and elevation angles). In this study, measurements at 630.0 nm were analyzed to study the thermospheric wind at the F-region altitude. Light of the airglow and aurora comes into the cooled charge-coupled device (CCD) camera (1024 × 1024 pixels) through an optical filter and etalon with a diameter of 116 nm. More than ten fringes can be captured simultaneously at each line-of-sight image due to the relatively wide field of view (the full width at half maximum is approximately 4°). The line-of-sight speed is derived from individual fringes and then averaged for each exposure. The statistical standard deviation in calculating the mean value is taken as the measurement uncertainty. Four cardinal points with a zenith angle of 15° and the geographic vertical (i.e., five directions) were measured sequentially, and the optical filters were switched between 557.7 and 630.0 nm every cycle. The exposure time at each position was 9 s for the 630.0-nm measurement, and one cycle with five directions took 80 s, including the data transfer time from the CCD sensor to the hard disk drive. To increase the signal-to-noise ratio, 2-by-2 binning was employed on the CCD image. The vector wind measurement at 630.0 nm was made every 140 s. The laser fringe measurement was obtained every 300 s. The combination of data from the four cardinal positions provides the horizontal components of the thermospheric wind velocity (Shiokawa et al. 2003, 2012).

Since this study deals with measurements taken during periods of geomagnetically quiet conditions, the

measurement uncertainties of the line-of-sight speed are likely large for some time intervals due to the relatively low optical emission intensity or signal-to-noise ratio. Therefore, a post-analysis with fringe image integration at each line of sight was applied and successfully improved the data quality. In this study, 4 and 20 fringe image integrations were performed, resulting in the time resolutions of the wind vector were 10 and 50 min, respectively. The figures shown in this study illustrate the integrated data.

All-sky cameras

This study analyzed all-sky images taken at four stations, Longyearbyen (Norway, geographic coordinates 78.15°N, 16.03°E), Abisko (Sweden, geographic coordinates 68.36°N, 18.82°E), Kilpisjärvi (Finland, geographic coordinates 69.05°N, 20.78°E), and Lovozero (Russia, geographic coordinates 67.97°N, 35.08°E), to capture auroral patterns in a wide area. Because of the low geomagnetic activity for this event, a major part of the auroral activity was localized at the northern edge of individual camera field of views (FOVs) at the three stations in Fennoscandia. Since the spatial resolution of the all-sky image tends to be inferior when approaching the edge, the auroral features captured by the three cameras during the event were almost identical. Auroral activities seen at Longyearbyen were at the southern edge of the FOV. Since aurorae appeared slightly closer to Longyearbyen than to the Fennoscandia sites, the structure was more clearly seen from Longyearbyen. Auroral dynamics and morphology were studied with images at 557.7 nm rather than those at 630.0 nm because of higher emission intensity and faster response to the particle precipitation that corresponds to the upward FAC pattern. We can expect that the forcing on neutral winds relative to the auroral pattern is similarly developed in space and time with concentrating around the 557.7-nm emissions originated in the E region. Therefore, camera images taken in Longyearbyen and Abisko at an optical wavelength of 557.7 nm were used to make plots in this study.

The camera at Longyearbyen is mounted with a low-cost Watec monochromatic sensor with a 557.7-nm optical bandpass filter and an all-sky lens (Ogawa et al. 2020). The exposure time was 1 s. The camera at Abisko and Kilpisjärvi belongs to the Magnetometers Ionospheric Radars All-sky Cameras Large Experiment (MIRACLE) camera network (Sangalli et al. 2011). The camera is equipped with an electron multiplying CCD (EMCCD) sensor. The exposure time of the 557.7-nm image was 0.8 s. The camera at Lovozero has been run

under collaboration with the Multiscale Aurora Imaging Network (MAIN) camera system operated by Polar Geophysical Institute (PGI) (Kozelov et al. 2012). The camera is equipped with a CCD camera at three optical wavelengths (427.8, 557.7, and 630.0 nm).

Dynasonde

Dynasondes have been used to estimate the ion velocity in the ionosphere by measuring the time series of the phase shift of the echo backscattered from various directions and altitudes. For the EISCAT Tromsø Dynasonde, the echoes returned from the virtual ranges of 300–500 km at frequencies of 2.8–8 MHz were used to estimate the ion velocity with the VFIT technique (Wright and Pitteway 1994). Dynasonde sounding was performed every 3 min. Sedgemore et al. (1996, 1998) compared the Dynasonde-measured ion velocity with the F-region ion velocity measured with the EISCAT ultrahigh frequency (UHF) tristatic method. Their event studies presented good agreement in a sudden change in the zonal component associated with the Harang discontinuity. This study focuses on a sudden zonal velocity change at a pseudobreakup, which is a similar situation to that examined in previous works.

IL/IU index derived from the IMAGE magnetometers

The International Monitor for Auroral Geomagnetic Effects (IMAGE) magnetometers (<https://space.fmi.fi/image>) were grouped into three areas by latitude (58.26–66.90°N, 68.02–71.09°N, and 74.50–78.92°N) in this study. Since two key instruments of this study, the FPI and Dynasonde, are located in Tromsø, Norway (69.58°N), the three latitudinal segments were named, from north to south, the “poleward side of Tromsø,” “near Tromsø,” and “equatorward side of Tromsø.” The regional AU and AL indices were estimated from measurements obtained in the individual segments (hereinafter written as IU and IL, respectively, which have been applied by, for example, Kauristie et al. (1996), Kallio et al. (2000) and Tanskanen et al. (2001)). This method has the advantage of identifying ionospheric current variations that may occur at higher latitudes during periods of geomagnetically quiet conditions, even if global AU and AL indices do not show notable signatures due to the large horizontal distance between the current density peak and the adopted magnetometer sites. Since this study focuses on an event appearing during a geomagnetically quiet period as presented in “Background of the solar wind and geomagnetic activity” section, IU and IL are more appropriate than AU and AL to identify ionospheric current activity.

Swarm

This study analyzed measurements of the electron density and electron temperature, which were derived from Langmuir probes (LPs) onboard the Swarm A and C satellites, and the field-aligned current, which was computed from individual magnetic field sensors. The ion velocity from the two thermal ion imager (TII) sensors, which are mounted on the Swarm A satellite and viewed in the horizontal and vertical planes, was also analyzed. Swarm A and C flew at a 435-km altitude during the event in this study. The LPs originally provided the electron density and temperature with a 2-Hz resolution, but the mean values with a 1-Hz resolution were analyzed in this study (Lomidze et al. 2018). The Level 2 field-aligned current (FAC) data products used in this study were estimated from the Swarm vector field magnetometer (VFM) data as described by Ritter et al. (2013) and are available from the data server (swarm-diss.esa.int). Although the Swarm A and C constellation is capable of estimating the FAC with the dual-satellite method, this study used values derived from the single satellite method, that is, the FACs were separately calculated from each spacecraft. Using the ion velocity measured from the TII horizontal and vertical sensors and the magnetic field measurements, the electric field perpendicular to the magnetic field was derived from the relation of $\mathbf{E} = -\mathbf{V} \times \mathbf{B}$. The TII sensors provide high-resolution ion distribution function images with a 16-Hz resolution, but the 2-Hz resolution data after onboard and further calibration processes on the ground were analyzed in this study (Knudsen et al. 2017).

Background of the solar wind and geomagnetic activity

The event in this study was analyzed to investigate an ephemeral red arc that appeared coinciding with a pseudo-breakup at geomagnetic latitudes of 71–72°N (Oyama et al. 2020). Figure 2 in Oyama et al. (2020) presents time series of the solar wind speed and density, plasmopause latitude, and geomagnetic indices. Therefore, this section does not repeat the details and provides an overall summary but important points for this study. After successive moderately low level of the solar wind speed for the first half of February 2018, high-speed solar wind streams (HSS) periodically reached the earth three times with peaks on 19, 23, and 27 February. The SYM-H index turned negative soon after the first HSS arrival, although only down to approximately -20 nT. This might not be counted as a geomagnetic storm. However, the Kp index increased synchronously with individual HSS arrivals. The event in this study was observed between the first and second HSS arrivals. For the event, the solar wind speed was approximately 400 km/s, slightly before reaching the minimum value after the first

HSS. The Kp index was 0+, and the plasmopause recovered from 56° to 63° geomagnetic latitude, which was still a slightly lower latitude than the quiet level of 65°. This event might be categorized in geomagnetically quiet conditions based on the Kp index value, but it is reasonable to propose that the magnetosphere still retained some energy to cause auroral activities as observed in northern Scandinavia for the event in this study.

Observations

Figure 1 presents the overall features of the ground-based measurement on the night of the event on 20 February 2018. The IU and IL indices, which are shown in Fig. 1a, b respectively, reveal that the magnitude of the ionospheric current was relatively small through the night. The IU and IL indices at the poleward side of Tromsø (blue) showed the largest magnitude in the three zones. This is consistent with the auroral pattern, which is displayed in the two keograms made from the all-sky cameras in Longyearbyen (Fig. 1c) and Abisko (Fig. 1d). The auroral activity was mainly concentrated at 75°–77°N through the night but moved closer to Longyearbyen before dawn. The Kp index was 0 to 1 throughout the night, as labeled in Fig. 1a, and was 0+ at 18–21 UT during the event in this study. From these ionospheric and auroral measurements, the geomagnetic activity can be classified at a low level, but a pseudo-breakup occurred at 18:35 UT in association with the development of the westward ionospheric current and brightening of the aurora. Slightly after the pseudo-breakup, an ephemeral red arc appeared at the equatorward side of the auroral arcs and its location was exactly at the ionospheric trough minimum (Oyama et al. 2020).

Figure 1e, f presents temporal variations in the FPI-measured zonal and meridional winds (solid circles with $\pm 1\sigma$, hatched gray), respectively, in Tromsø, Norway. For reference, thermospheric winds at a 250-km height from the horizontal wind model (HWM) are overlaid by the green line (Hedin et al. 1996). The HWM-modeled wind reasonably captures the measurements, particularly for the meridional component. For the zonal component, there are discrepancies in the measurement for the first several hours and around midnight. Of particular interest is the gradual westward acceleration of the wind seen at approximately 18 UT. The acceleration seems to begin before the commencement of auroral brightening and negative bay development in the IU and IL indices. This is an important point in this study, and was examined carefully using wind data with a higher time resolution, as presented in Fig. 3.

For the time period of interest in this study, the Tromsø Dynasonde received tolerable signals to estimate the horizontal ion velocity in the F region. The majority of

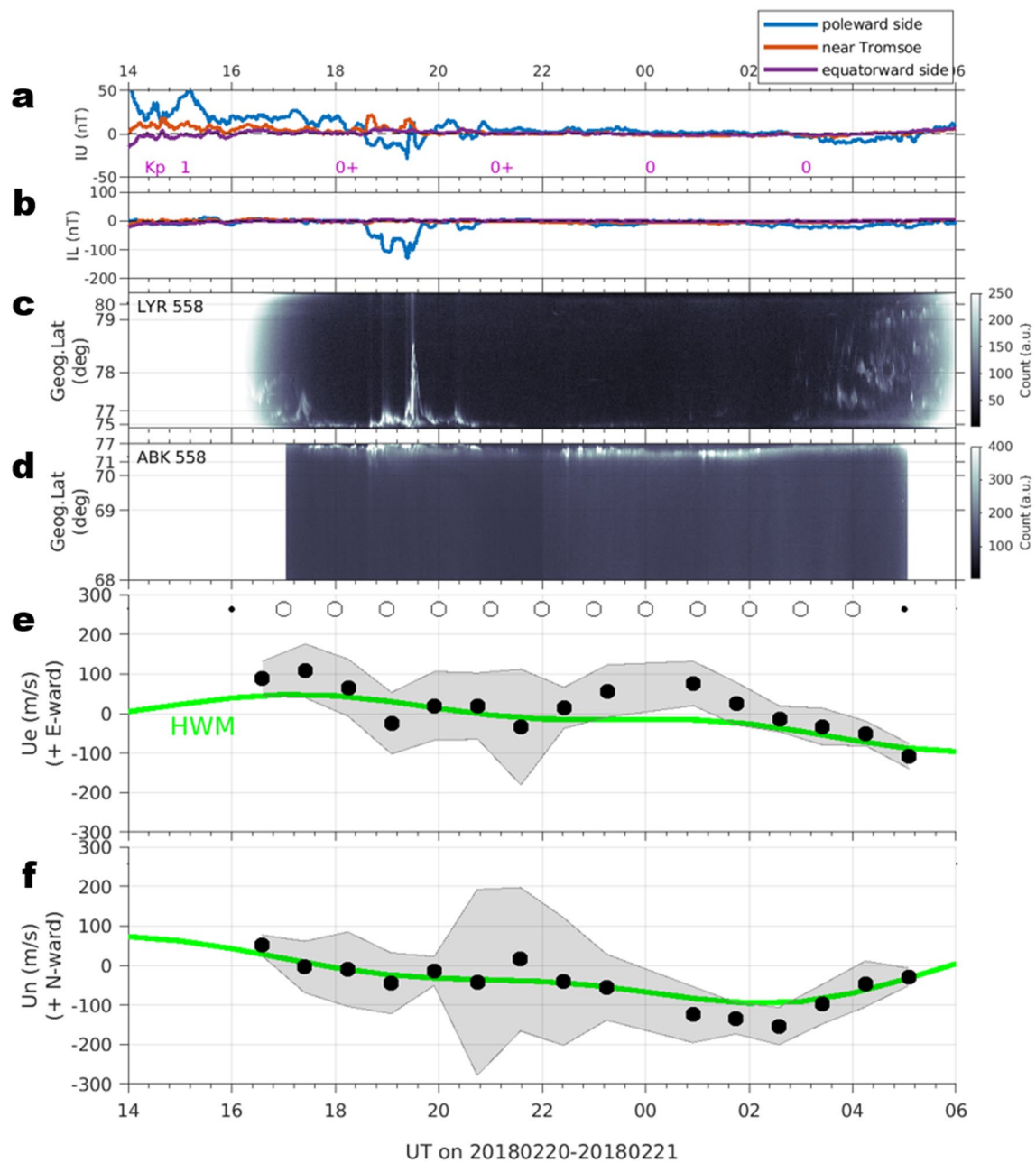


Fig. 1 Measurements on 2018 February 20–21 of **a, b** IU and IL indices made of IMAGE magnetometers segmented into three areas (poleward (blue; 74.50–78.92°N), near (orange; 68.02–71.09°N) and equatorward (purple; 58.26–66.90°N) side of Tromsø (69.58°N)), **c, d** keograms made using the all-sky camera (558 nm) at Longyearbyen and Abisko, respectively, and **e, f** zonal and meridional components (positive eastward and northward, respectively) of the thermospheric wind velocity measured with the FPI at Tromsø (630 nm). Post-integration of 20 FPI fringe images, corresponding to a 50 min time resolution of the wind vector (black solid circles), was applied to the original images taken every 2.5 min. The error bars for each wind component ($\pm 1\sigma$) are shown in shading. HWM winds at 250-km altitude are overlaid (green curves). The Kp index every 3 h is marked in **(a)**

the echo reflection was located within a horizontal distance of 50 km from the zenith, although a fraction was expanded northward by approximately 200 km. The FPI wind from the four oblique directions at a 15° zenith angle was derived assuming a uniform wind pattern

within 67 km from the zenith at 250-km altitude. It is therefore considered that the Dynasonde measured the ion velocity in approximately the same volume as the FPI. Figure 2c, d presents time series of the zonal and meridional components, respectively, of the ion velocity

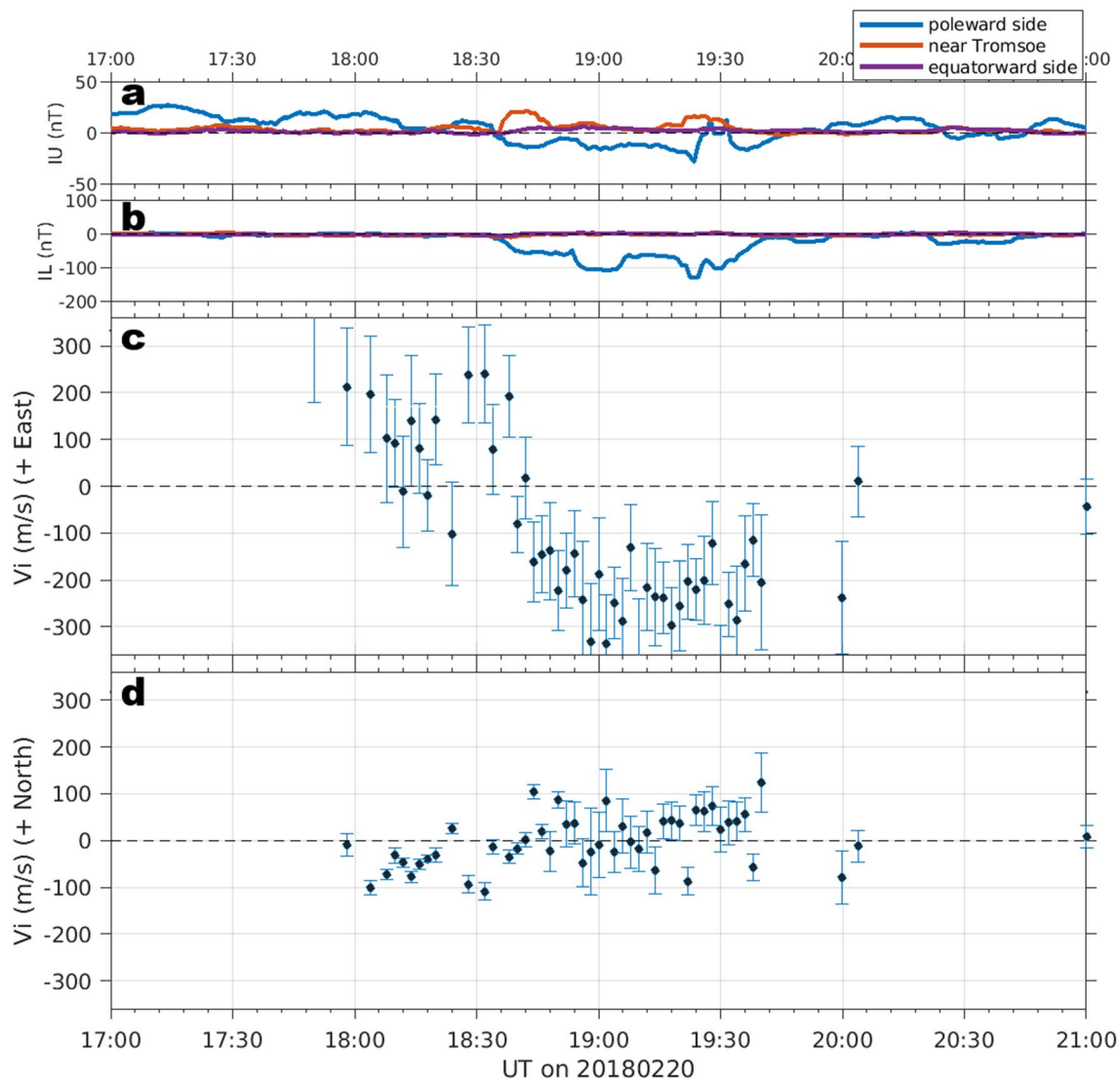


Fig. 2 **a, b** The same as in **a, b** of Fig. 1 but from 17 to 21 UT on 2018 February 20. **c, d** The zonal and meridional components of the ion velocity measured with the Tromsø Dynasonde from 17 to 21 UT on 2018 February 20 (positive eastward and northward, respectively). The measurement uncertainty ($\pm 1\sigma$) is illustrated by vertical bars

with $\pm 1\sigma$ error. Figure 2a, b presents IU and IL indices, which are identical to the values shown in Fig. 1a, b respectively, but for time period of 17–21 UT. Slightly after 18:30 UT, synchronizing with the development of the negative bay in the IU and IL indices at the poleward side of Tromsø (blue), there was a strong turning of the plasma westward and a more gradual turning northward within 10 min.

Figure 3d presents a comparison between the FPI-measured wind (4 fringe image integration or 10-min time resolution) and the Dynasonde-measured ion velocity. The IU and IL indices (Fig. 3a, b) are identical to those in Fig. 2a, b, respectively. The keogram shown in Fig. 3c

was made from the same dataset as for Fig. 1c but focuses on the event time and latitudes with the auroral activity. The measurement uncertainty with $\pm 1\sigma$ is indicated by a vertical bar at individual measurements for the ion velocity (orange in Fig. 3d). For the neutral wind, the mean measurement uncertainty for the time period is presented on the left-hand side of Fig. 3d. The neutral wind measurement uncertainty is moderately large even after the four fringe image integrations because of the low emission intensity, as expected from Fig. 1d (see measurements at the Tromsø latitude or approximately 70°N). However, the derived wind values show a trend of westward acceleration from 18:15 to 19:00 UT, which was also

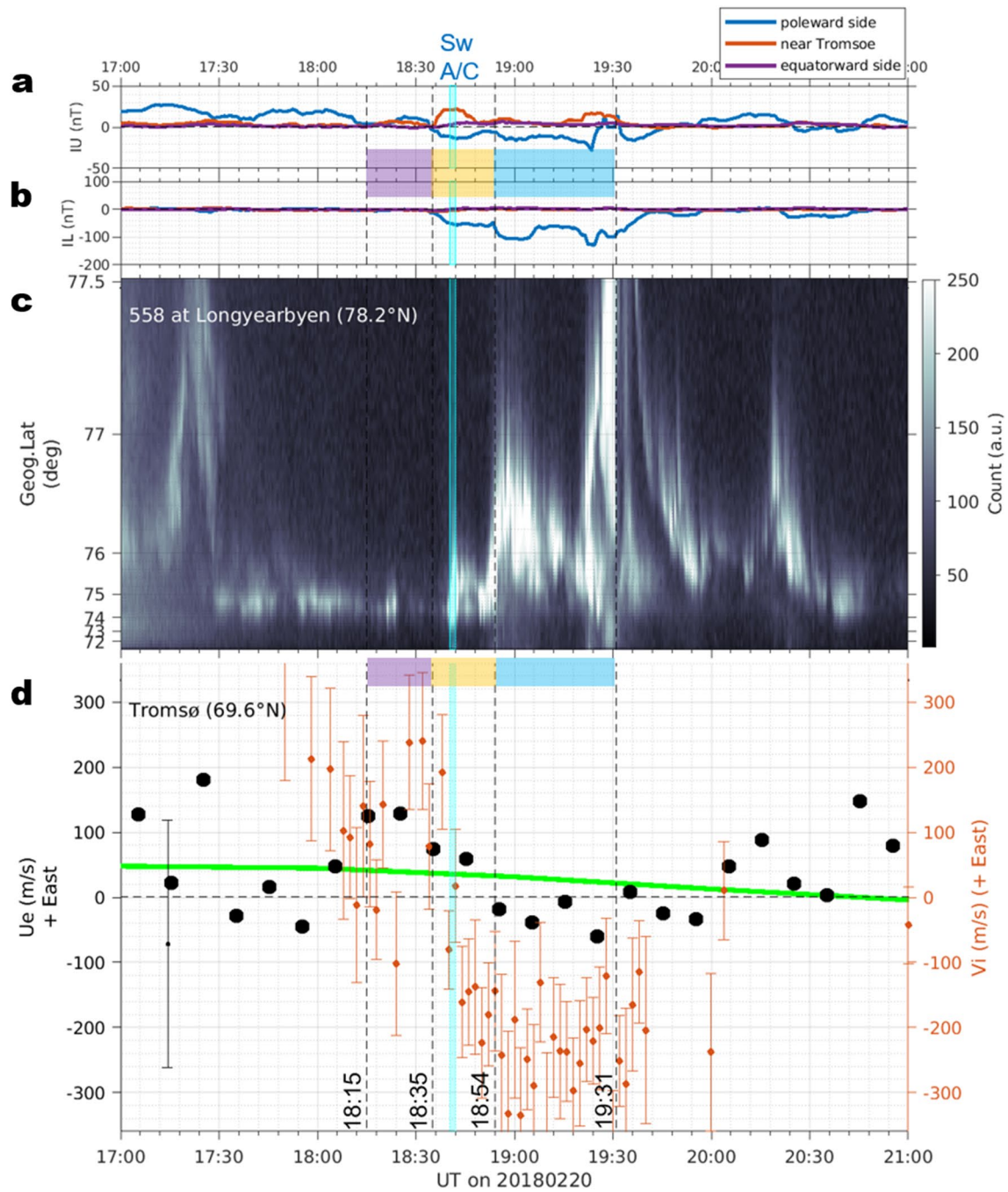


Fig. 3 Time series of **a** IU, **b** IL, **c** keogram made of the all-sky camera at Longyearbyen (but from 72 to 77.5°N) and **d** zonal component of the FPI-measured neutral wind (black dots) and ion velocity from the Dynasonde (orange dots) at Tromsø from 17 to 21 UT on 2018 February 20. Post-integration of 4 FPI fringe images was applied, corresponding to a 10-min time resolution. The mean error of the neutral wind for the selected four hours is illustrated by a black vertical bar. Individual errors of the ion velocity are marked by orange vertical bars. The green curve represents the HWM zonal wind at 250-km altitude. The time of the Swarm pass over Scandinavia is marked by a vertical light blue bar, which is drawn from 18:40:18 to 18:42:08 UT, corresponding to the shifted geographical latitude from 67 to 74°N (see Fig. 4c). The time interval from 18:15 to 19:31 UT is separated into three groups, highlighted in purple, yellow, and light blue. These colors are also applied in Fig. 6 to highlight individual time intervals

observed in Fig. 1e made of the 20 fringe image integration and smaller measurement uncertainties. Therefore, we discuss the wind variations referring to the results from the 4 fringe image integrations. In comparing these measurements, the time interval from 18:15 to 19:31 UT was grouped into three periods, as highlighted by colored bars (purple: 18:15–18:35 UT; yellow: 18:35–18:54 UT; light blue: 18:54–19:31 UT). These three time segments were defined based on the magnetic field and auroral signatures, which are presented in Fig. 3a–c. The time interval of 18:15–18:35 UT (purple) corresponds to the last 20 min of the growth phase as characterized by positive IU values at the poleward side and near the Tromsø area, together with a moderately stable appearance of the aurora at 74–75°N, which is the most equatorward latitude before the pseudo-breakup at 18:35 UT. The time interval of 18:35–18:54 UT (yellow) corresponds to the first 19 min of the expansion phase, in which development of the eastward and westward ionospheric currents occurred near the Tromsø area and the poleward side, respectively, coinciding with a sudden brightening seen in the keogram. The time interval of 18:54–19:31 UT (light blue) is the later part of the expansion phase, including the poleward drift of the bright aurora. The time interval of the Swarm A and C spacecraft flying over

northern Scandinavia is highlighted by a vertical narrow light blue bar, which is examined in Fig. 4.

For the time interval of 18:15–18:35 UT (purple), zonal components of the ion velocity and neutral wind are positive (eastward), except for a single ion velocity measurement of -102 m/s at 18:24 UT. This remarkable negative value coincides with a conspicuous brightening seen in the keogram, although the ion velocity measurement was obtained a few hundred kilometers equatorward from the auroral brightening. Although it was difficult to discern the precise horizontal pattern of the aurora in the original all-sky image because of the limitation of the spatial resolution near the edge of the camera FOV, a few bright blobs drifted westward. This feature is similar to auroral beads, which can occur immediately before substorm onset (Sakaguchi et al. 2009; Hosokawa et al. 2013). The upward FAC flowing out from the bright blobs might be associated with the poleward electric field or the ionospheric closure current at the equatorward side, which could drift the ionospheric ions to the $\mathbf{E} \times \mathbf{B}$ direction or westward in the F region. The neutral wind was accelerated eastward before 18:15 UT, but the acceleration paused concurrent with the spontaneous auroral brightening and the sudden westward turning of the ion velocity at 18:24 UT. Then, the wind acceleration

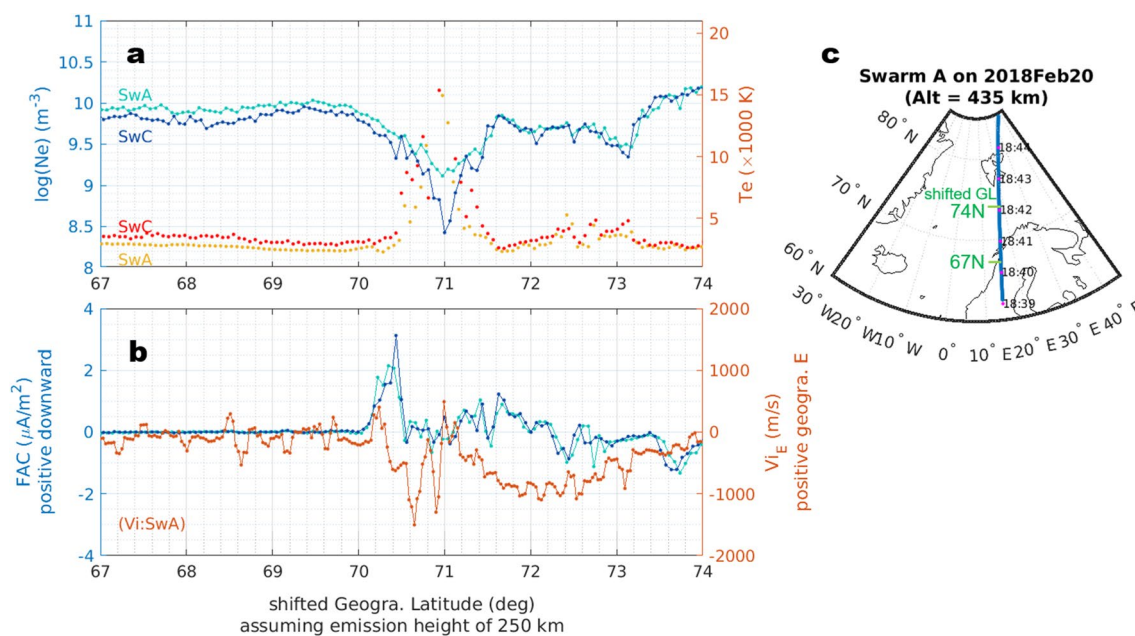


Fig. 4 **a** Electron density and temperature (cold and warm hues, respectively) measured with the Swarm A (lighter color) and Swarm C (darker color) satellites. **b** FAC and eastward ion velocity (cold and warm hues, respectively; positive downward and eastward, respectively) measured with the Swarm A (lighter color) and C (darker color) satellites. The latitude at the Swarm measurement is shifted by 0.39–0.28° (dependent on latitudes at 67–74°N) poleward while being mapped down along the magnetic field line from the operation altitude of 435 km to the assumed 630-nm emission height of 250 km. **c** Swarm A trajectory on the map with time stamp. Locations of the shifted geographical latitudes of 67° and 74° are marked as references

shifted westward, although the zonal ion velocity turned eastward following a fleeting mitigation moment of auroral activity. These trends suggest that the force acting on the thermosphere at Tromsø latitudes turned westward at 18:24 UT rather than ceasing. The westward acceleration of the wind lasted until the end of the time segment highlighted by yellow, although the first several measurements of the ion velocity are eastward. For the last 12 min of the second part (i.e., from 18:42 to 18:54 UT), the ion velocity was westward, but the neutral wind was still eastward. This means that the thermospheric neutral and ionospheric plasma flows were approximately antiparallel, which is an important observational result in this study. As highlighted by a narrow vertical light blue bar, the Swarm satellites passed over the Tromsø–Longyearbyen line (see Fig. 4c) at an exact moment that the plasma flow turned from eastward to westward. The zonal ion velocity may be in a period of the transition, as two Dynasonde measurements were at a sharp edge of the time segments prevailing with positive and negative measurements. Furthermore, the Swarm pass was also right on the time of auroral brightening at 73–76°N (see Fig. 3c). For the third part highlighted by light blue (18:54 to 19:31 UT), the ion velocity remained westward with a moderately stable magnitude of approximately from -200 to -300 m/s, and the neutral wind direction also stayed westward.

Latitudinal profiles of measurements from the Swarm A and C spacecraft are presented in Fig. 4. Latitudes of the Swarm measurements at a 435-km altitude were shifted by mapping individual satellite locations down to 250 km along the magnetic field. Values of the measurement have not been modified in the mapping procedure. The electron density, shown in Fig. 4a in bluish hue, presents a sharp depression centered at 71°N, along with a peak electron temperature reaching 15,000 K. These contrastive features are often seen in the ionospheric trough, and an ephemeral red arc was found at the latitude of the trough minimum during this event (Oyama et al. 2020). The overall profiles of the electron density and temperature are almost identical between the Swarm A and C measurements. However, looking at the fine structures, some discrepancies between the two measurements are apparent, for example, in the electron density at the trough minimum (i.e., higher values from Swarm A than Swarm C), which might be attributed to measurements during the period of the ionospheric transition, as mentioned above. We can assume that the overall pattern represents ionospheric spatial structures rather than temporal variations but likely encompasses temporal variations in the fine structure. At latitudes higher than 73°N, there is a bump in the electron density, which is attributed to auroral precipitation with softer

electrons than the auroral electrons represented in the keogram (Fig. 3c). The FPI and Dynasonde measurements in Tromsø were made around latitudes centered at 69.6°N, which is located at the edge of the equatorward side slope of the trough. The zonal component of the ion velocity measured with Swarm A (Fig. 4b; orange) has two negative peaks in the trough region at 70.65° and 70.90° shifted geographic latitude. These zonal plasma flow patterns with double peaks may be DSAID (Horvath & Lovell, 2017) in the case of spatial patterns rather than temporal variations, but they would be hard to distinguish because the measurement was obtained during rapid ionospheric development. These peaks are located on the equatorward side slope of the trough. On the poleward side slope and beyond, the westward flow expands to the auroral region. Of particular interest is an eastward counter flow, which was found at the trough minimum at 71°. This is in contrast to the SAPS or plasma flows generated by the poleward polarization electric field linking the R1 and R2 FACs. The eastward flow in the trough was also found in a narrow region at approximately 70.2° shifted geographic latitude. The FAC estimated from the Swarm A and C magnetic field measurements (Fig. 4b; blue hue) tends to be dominantly downward at the trough latitude, but has many small-scale structures. There is a large downward FAC peak (at 70.4° shifted geographic latitude) at the equatorward side of the trough minimum, reaching 2–3 $\mu\text{A}/\text{m}^2$. At latitudes between the FAC peak and the trough minimum, the FAC magnitude is moderately small in positive or downward directions, and the structured plasma flows are localized in this region. At the poleward side from the trough minimum to the auroral region starting at approximately 73°, the dominant FAC direction shifts from downward to upward with increasing latitudes, and the westward ion flow peaks near latitudes where the FAC direction reverses.

Discussion

In this study, the ionosphere and thermosphere around the ionospheric trough at dusk were measured from the ground and space during a geomagnetically quiet period of $K_p=0+$. The Dynasonde and FPI collocated in Tromsø, Norway measured the equator side edge of the ionospheric trough and presented temporal evolutions of the ionospheric and thermospheric dynamics, respectively, at the F-region altitude. Coinciding with a pseudo-breakup at 18:35 UT on 20 February 2018, there was a strong turning of the plasma westward and a more gradual turning northward within 10 min, changing the zonal direction several times. The FPI-measured wind accelerated westward in response to the plasma flow change but with slower development than the ion velocity, with the thermospheric wind remaining eastward for a while

after the pseudo-breakup. The most likely mechanism of the change in the wind direction is ion drag, which transfers momentum from ionospheric ions to thermospheric neutral particles through collisions. Ion drag is a slow process of momentum transfer, as described by the e-folding time, which has been adopted to represent the time constant of momentum transfer (Baron and Wand 1983; Deng et al. 2009). The thermospheric wind cannot instantly follow a sudden change in the ion velocity due to thermospheric inertia, which may cause approximately opposite flows between ions and neutral particles for a while immediately after the ion velocity change. This situation can occur at the substorm onset when the magnetospheric electric field suddenly rotates from poleward to equatorward. The sporadic westward turning of the ion velocity at 18:24 UT (see Fig. 3d) is a good example to examine the development of thermospheric dynamics during a sudden ionospheric change.

This section compares the ion velocity and neutral wind vectors to examine the role of thermospheric wind in the energy dissipation process. Most of the time, the electromagnetic energy flux of magnetospheric origin flows into the ionosphere, resulting in conversion to thermal and kinetic energies through the Joule heating process and the Lorentz force, respectively. The conversion is localized in a moderately narrow altitude region of 100–300 km compared with, for example, the auroral electron acceleration region (Imajo et al. 2021 and references therein), which is a transition region from a collision-dominant region in the ionosphere to a collision-free region in the magnetosphere. This study investigated the transition region near the border of the collision-free region. The energy transfer process from the ionosphere to the thermosphere at high latitudes has been studied by applying the following equation:

$$\mathbf{J} \cdot \mathbf{E} = \mathbf{J} \cdot \mathbf{E}' + \mathbf{U} \cdot (\mathbf{J} \times \mathbf{B}), \quad (1)$$

where $\mathbf{E}' = \mathbf{E} + \mathbf{U} \times \mathbf{B}$ is the electric field as measured in a reference frame moving with the neutral wind, and \mathbf{E} , \mathbf{U} , \mathbf{J} , and \mathbf{B} are vectors of the electric field, neutral wind, ionospheric current density, and magnetic field, respectively (Brekke and Rino, 1978; Thayer et al. 1995; Fujii et al. 1998; Aikio et al. 2012). The source region where energy is transferred from plasma to the electromagnetic field is generally in the magnetosphere, resulting in a negative $\mathbf{J} \cdot \mathbf{E}$. Since the energy should be dissipated in the sink region or the high-latitude ionosphere, the energy is transferred from the electromagnetic field to the ionospheric plasma with positive $\mathbf{J} \cdot \mathbf{E}$. Assuming that σ_H/σ_P (σ_P and σ_H are the Pedersen and Hall conductivities, respectively) is much smaller than 1 in the F region (see Fig. 4 of Richmond and Thayer, 2000) and that the electric field is perpendicular to \mathbf{B} , $\mathbf{J} \cdot \mathbf{E}$ can be written as

$$\mathbf{J} \cdot \mathbf{E} = \sigma_P E^2 - \sigma_P B^2 \mathbf{U} \cdot \mathbf{V}. \quad (2)$$

The first term of the right-hand side is always positive, but the sign of the second term is dependent on $\mathbf{U} \cdot \mathbf{V}$. Since $\mathbf{J} \cdot \mathbf{E}$ represents electromagnetic work, magnetosphere-originated energy is dissipated for Joule heating and Lorentz force in the ionosphere. The thermospheric wind flows after the ionospheric ion velocity, and in most cases, the thermospheric wind is approximately parallel to the ionospheric ion velocity at the F-region altitude, particularly at the dusk side (Richmond et al. 2003; Xiong et al. 2015; Dhady et al. 2018). It is thus expected that $\mathbf{U} \cdot \mathbf{V}$ in the F region remains positive most of the time. However, in the case where \mathbf{V} suddenly changes direction, neutral particles, which are unbounded by the magnetic field, do not instantly follow ionospheric plasma drifts due to thermospheric inertia. The slow thermospheric response fosters the velocity difference between \mathbf{V} and \mathbf{U} , resulting in a Joule heating energy temporarily larger than that supplied from the magnetosphere. This situation may occur when the electric field of the magnetospheric origin suddenly decreases or spatiotemporally changes its direction. The relative speed between \mathbf{V} and \mathbf{U} would decrease with time through gradual momentum transfer between ions and neutrals if a constant ion drag is in effect. The time constant, which relates to the e-folding time, may be several tens of minutes and dependent on altitude or the neutral and ionized particle densities. For the transition time, $\mathbf{U} \cdot \mathbf{V}$ may remain negative, which increases the Joule heating rate in addition to the magnetospheric energy input. From Eq. (2), $\mathbf{J} \cdot \mathbf{E}$ is larger than $\sigma_P E^2$ when $\mathbf{U} \cdot \mathbf{V}$ is negative. Thermospheric wind effects on the Joule heating rate have been studied at mainly E-region altitudes with examining a term of $\mathbf{U} \cdot (\mathbf{E} \times \mathbf{B})$ (Lu et al. 1995; Thayer, 1998). Since ions in the E region move off $\mathbf{E} \times \mathbf{B}$ direction due to collisions with neutral particles, $\mathbf{U} \cdot (\mathbf{E} \times \mathbf{B})$ is not identical with $\mathbf{U} \cdot \mathbf{V}$. Therefore, knowledge about the thermospheric wind effect at E-region altitudes cannot be simply applied to the F-region altitudes. The sign of $\mathbf{U} \cdot \mathbf{V}$ was calculated in an ion-neutral coupling study (Kiene et al. 2018, 2019) and was evaluated to study the roles of the thermosphere in the energy dissipation process. However, due to paucity of measurements, $\mathbf{U} \cdot \mathbf{V}$ in the F region has not been well studied yet.

A diagram of Fig. 5 may be helpful to capture an abstract principle on larger Joule heating for the negative $\mathbf{U} \cdot \mathbf{V}$ case than positive one. In this theoretical argument, we set four assumptions to focus on \mathbf{E} direction change: 1) no change in $|\mathbf{E}|$, 2) ionospheric conductivity is uniform in space and time, 3) the background magnetic field \mathbf{B}_0 is downward and 4) $|\mathbf{E}| > |\mathbf{U} \times \mathbf{B}_0|$. One may complain to the assumption #1 because the magnetospheric energy input may increase during period of the negative

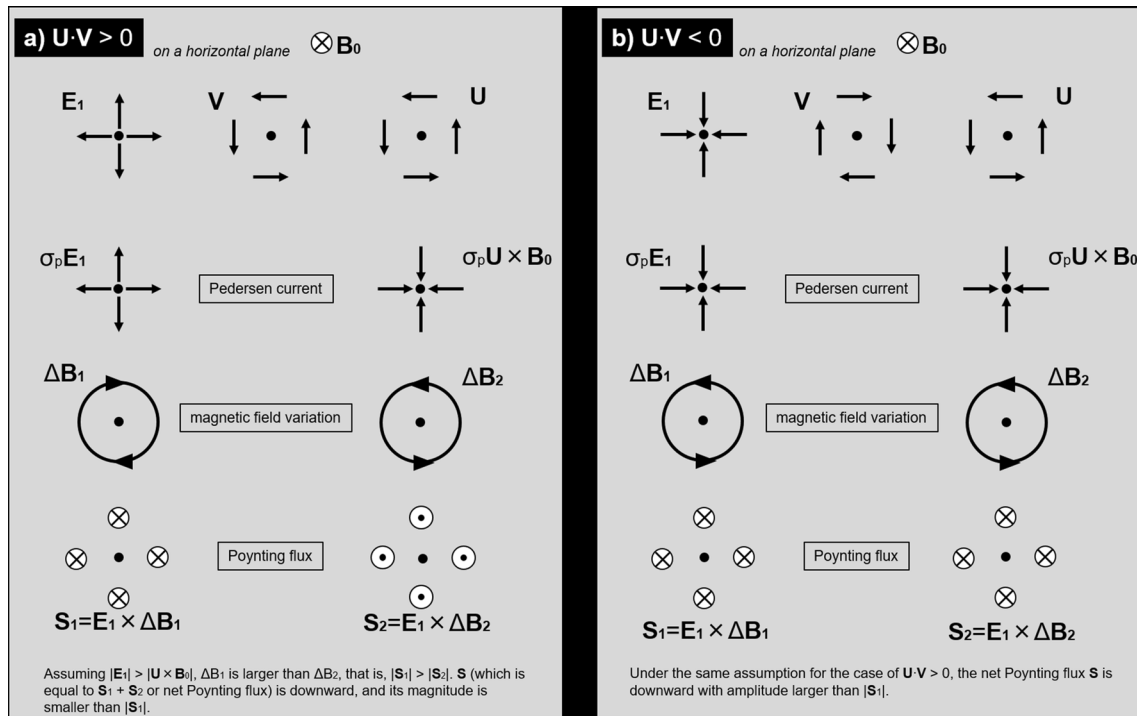
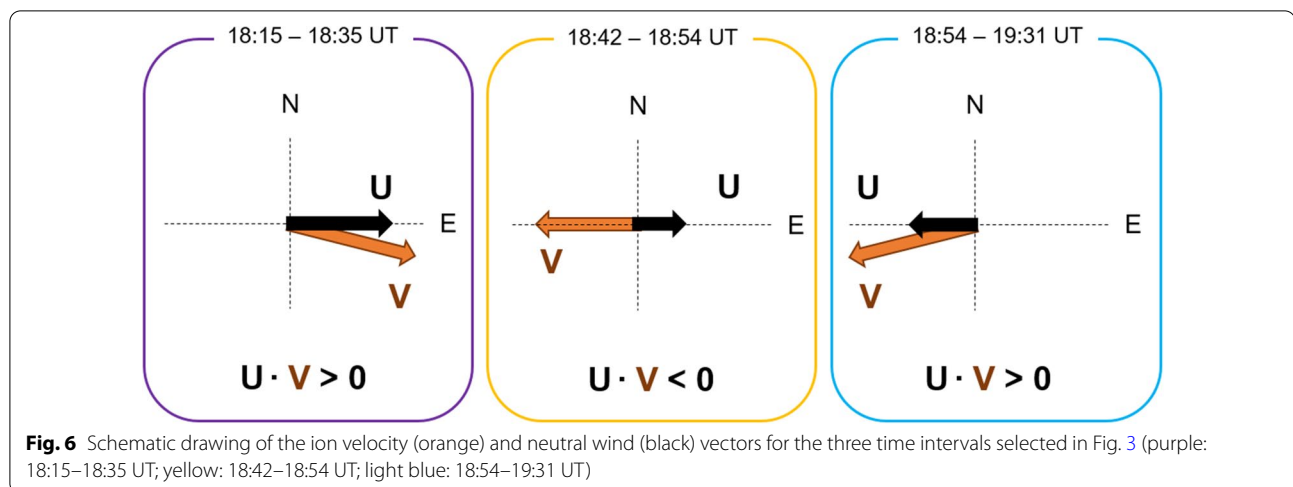


Fig. 5 A conceptual diagram of direction of the Poynting flux for the case of **a** positive and **b** negative $U \cdot V$

$U \cdot V$. However, in order to focus on thermospheric wind contributions, Fig. 5 ignores the magnitude change. The assumption #4 is mostly acceptable at high latitudes for periods with auroral activities. On a horizontal plane in the F region, let us assume counter-clockwise rotating V and U for the positive $U \cdot V$ case (panel a). Since the Pedersen term of the current is dominant in the F region, the currents driven by E and U shall be divergent and convergent, respectively, resulting in clockwise and counter-clockwise magnetic field disturbances, respectively. Therefore, the Poynting flux related to E , S_1 , is downward, and that related to U , S_2 , is upward. Since $|S_1|$ is larger than $|S_2|$ according to the assumption #4, the net Poynting flux, S , is downward and its magnitude is smaller than $|S_1|$ by $|S_2|$. For the negative $U \cdot V$ case (panel b), E reverses, resulting in clockwise V but U may still remain anti-clockwise due to the thermospheric inertia. Through the same procedure as the positive $U \cdot V$ case, both S_1 and S_2 are downward. The net Poynting flux, S , is downward and its magnitude is larger than $|S_1|$ by $|S_2|$. In summary, the net Poynting flux is downward for both cases, but the magnitude, $|S|$, is larger for the negative $U \cdot V$ case than the positive case despite no changes in the electric field magnitude and the ionospheric conductivity.

The sign of $U \cdot V$ for the selected three time intervals presented in Fig. 3 is interpreted in Fig. 6. Figure 6 illustrates the approximate magnitude and direction

of V and U , representing measurements for individual time intervals. For the last 20 min before the pseudo-breakup (highlighted by a purple rectangle) and for the last 37 min of the expansion phase (highlighted by a light blue rectangle), the sign of $U \cdot V$ is positive because the neutral wind U and ion velocity V are approximately parallel. It is thus considered that the electromagnetic energy of magnetosphere origin was converted to Joule heating and Lorentz force. It is noted that there can be exceptions, such as the event with a sporadic westward turning of the ion velocity at 18:24 UT (see Fig. 3d), which should provide negative $U \cdot V$. On the other hand, for the time interval between the two, which is highlighted by a yellow rectangle in Fig. 6, the sign of $U \cdot V$ is negative because the vectors are approximately antiparallel. This happens during the expansion phase but not immediately after pseudo-breakup. Since a negative sign was found during the period of a sudden direction change in the ion velocity from eastward to westward coinciding with pseudo-breakup, the thermospheric wind could not follow the sudden change due to inertia. According to discussion with Fig. 5, it is considered that larger Joule heating energy is generated additionally from the magnetospheric energy inputs. The particle collision also causes deceleration of V . The thermospheric wind effect is attributed to an



irresistible force of the thermosphere rather than due to energy balance in the magnetosphere-ionosphere coupled system in a similar manner to the flywheel effect, which is triggered by a sudden termination of the current flow between the magnetosphere and the ionosphere after developing a plasma-convection-like pattern in the thermospheric wind (Richmond, 1995).

Measurements in this study were obtained at the F-region altitude, and there is no measurement in the E region. Since the altitude region for converting the electromagnetic energy flux of magnetospheric origin to the thermal and kinetic energies in the ionosphere is distributed down to the E region, this study cannot reveal the complete thermospheric role in the energy conversion process. However, it may be a challenging analysis to derive the Poynting flux from conjugated Swarm measurements. The direction of the energy flow can be examined by the Poynting flux (Thayer et al. 1995; Mishin et al. 2003; Streltsov and Mishin 2003; Pfaff 2012; Vanhamäki et al. 2012; Rodriguez-Zuluaga et al. 2017). Measurements with the Swarm A spacecraft were conducted along the approximate Tromsø-Longyearbyen line from 18:40:18 to 18:42:08 UT, as shown in Fig. 4c. This is remarkably close to the beginning of the period with negative $\mathbf{U} \cdot \mathbf{V}$, as shown in Fig. 3c. The Poynting flux was calculated from measurements of the magnetic field and the ion velocity with Swarm A. Perturbations of the magnetic field, $\Delta \mathbf{B}$, were derived by subtracting values calculated with the CHAMP, Ørsted, and SAC-C model of Earth's magnetic field (CHAOS-7) (Finlay et al. 2020). The electric field, \mathbf{E} , was derived from measurements of the ion velocity from the horizontal (H) and vertical (V) sensors of TIIs and the magnetic field. Technically speaking, two kinds of the electric field vector can be obtained depending on which of the along-track measurements

is applied. Then the Poynting flux was obtained from $\mathbf{E} \times \Delta \mathbf{B} / \mu_0$, where μ_0 is the permeability of free space. Figure 7a–c presents the latitudinal profiles, which are the same as those shown in Fig. 4a, b but for Swarm A measurements. The calculated Poynting flux (positive downward) is shown in Fig. 7d. Error values with $\pm 3\sigma$ are indicated in red (blue) for the results with the along-track measurements from the H (V) sensor. In this study, we accepted the sign of the Poynting flux to indicate energy flow direction only when both values derived from the H and V sensors have the same sign, taking into account an error of $\pm 3\sigma$.

The Poynting flux at latitude of Tromsø or 69.6° was smaller than 6σ , and it was difficult to determine the sign according to the definition mentioned above. The simultaneous FPI-Dynasonde measurement presented negative $\mathbf{U} \cdot \mathbf{V}$ in the F region, which suggests increase in Joule heating. If this were the case for the whole thermosphere at 100–300-km altitude, some amount of the wind-generated energy might flow out to the magnetosphere. However, measurements analyzed in this study were conducted at limited altitudes in the F region, and there is no measurement at other altitudes. Since \mathbf{U} and \mathbf{V} can vary with heights (Larsen, 2002; Sect. 7.2 of Brekke, 2013), we cannot evaluate energy flow direction from $\mathbf{U} \cdot \mathbf{V}$ in the F region alone.

In the ionospheric trough and subauroral region, that is, at latitudes from 70° to 73° , the dominant direction of the Poynting flux is downward with westward ion velocity (see Fig. 7c, d). On the other hand, a salient finding is the negative or upward Poynting flux at latitudes of 71° , which corresponds to the trough minimum (Fig. 7a) and collocates with the localized eastward flow (Fig. 7c). The eastward plasma flow is surrounded by westward flows at both the equatorward and poleward sides. The eastward

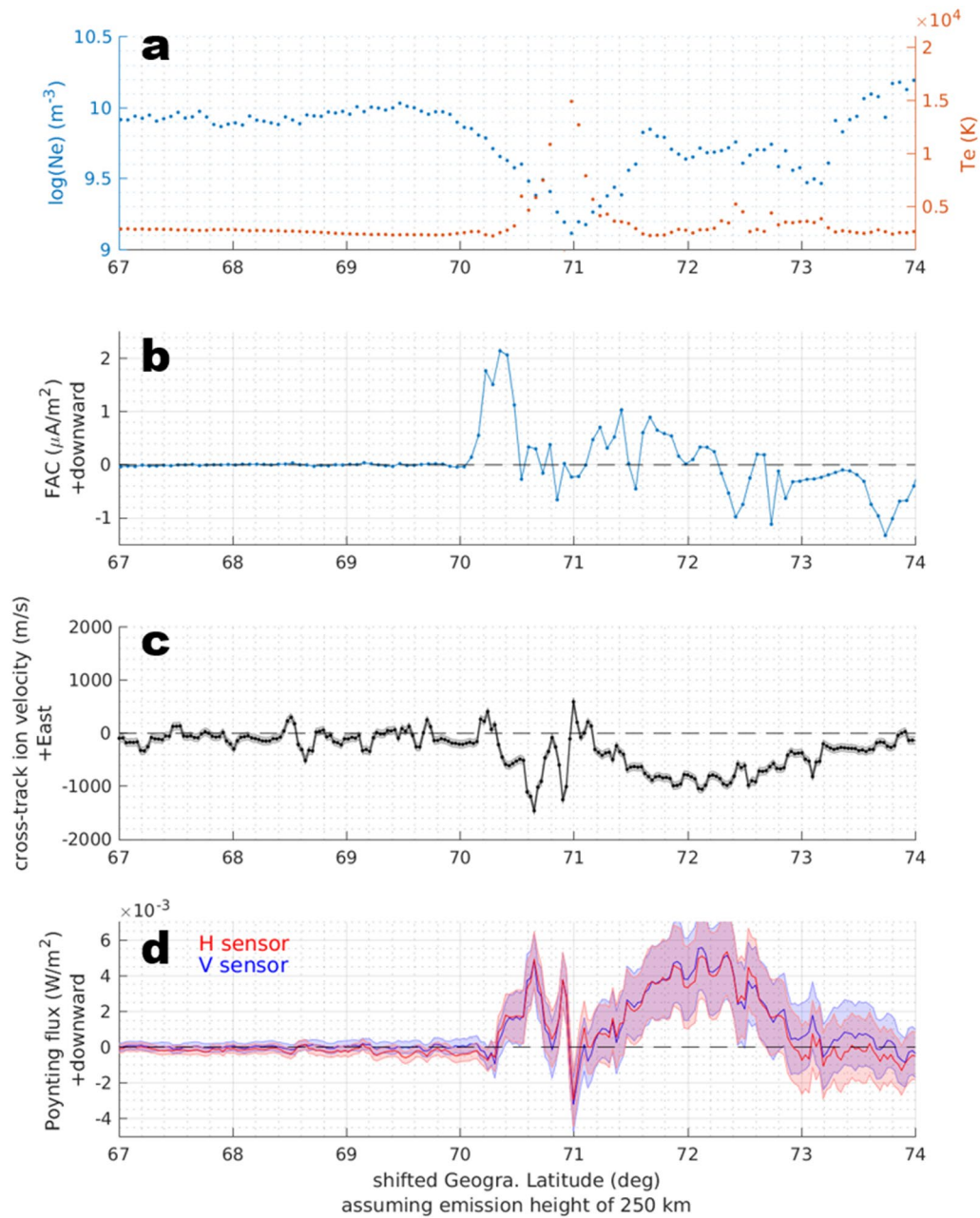


Fig. 7 Swarm A measurements of the **a** electron density and temperature (same as Fig. 4a), **b** field-aligned current (FAC; positive downward; same as Fig. 4b) and **c** ion velocity (positive eastward; same as Fig. 4b). **d** Poynting flux derived from Swarm A measurements of the ion velocity and magnetic field (positive downward) with error values of $\pm 3\sigma$. Calculations were made applying the along-track ion velocity from the horizontal (H; red) and vertical (V; blue) sensors, filtered by a 3-point moving average. The horizontal axes of all the panels were shifted in the same way as in Fig. 4

plasma flow at the trough minimum has been observed in measurements during previous and successive Swarm passes over northern Europe (see EPS Additional file 1); it is thus not regarded as a coincidence and may imply a spatial structure rather than temporal variations. Since there was no thermospheric wind measurement at the

trough minimum for this event, it is just an estimation but the thermospheric wind can likely flow westward in the SAPS region, as demonstrated by Wang et al. (2011, 2012a, b). Since the eastward plasma flow region at the trough minimum is much narrower in latitude than the latitudinal width of the westward plasma flows, it

is reasonably acceptable to assume that an eastward counterstream of the thermospheric wind could not be well developed by the eastward plasma flows due to the thermospheric inertia. The thermospheric wind barely follows the fine structures instantaneously in the ionospheric dynamics. Molecular viscosity is predominant at F-region altitudes, at which the molecular viscosity coefficient is considerably larger than the eddy diffusion coefficient. A larger molecular viscosity leads to a uniform distribution of the momentum. This trend becomes stronger with altitude because the molecular viscosity coefficient is inversely proportional to the neutral density. If this is the case, $U \cdot V$ may have been negative at the trough minimum in the F region, resulting in larger Joule heating than the surrounding areas.

Conclusions

This study focused on the event on 20 February 2018 and analyzed ionospheric and thermospheric measurements obtained with ground-based and spaceborne instruments in the northern Scandinavian area (65–80°N). During the event, geomagnetic activity was considerably low ($K_p=0+$), but there was some auroral activity at the higher latitudes (73–77°N), and the ionospheric trough appeared at latitudes of 70–72°N. The meridional distance between the aurora and the ionospheric trough was approximately 200–600 km. Of particular interest was the ion-neutral particle interaction, which was deduced from the westward acceleration of the thermospheric wind at the equatorward edge of the ionospheric trough, coinciding with a sudden westward turning of the ion velocity at a pseudo-breakup. The simultaneous FPI–Dynasonde measurement revealed negative $U \cdot V$ in the F region for a period immediately after pseudo-breakup with opposite directions of U and V . Theoretical examination suggested larger Joule heating for the case of negative $U \cdot V$ than positive $U \cdot V$. Poynting flux from a Swarm flyover during the event supported this hypothesis. The sign of $U \cdot V$ may be used as an indicator to determine the time and location where thermospheric inertia plays a role in the energy dissipation process.

Abbreviations

FPI: Fabry–Perot interferometer; SAPS: Subauroral polarization stream; R1: Region 1; R2: Region 2; FAC: Field-aligned current; DSAID: Double-peak subauroral ion drift; DMSP: Defense Meteorological Satellite Program; CHAMP: Challenging Minisatellite Payload; EISCAT: European Incoherent Scatter; CCD: Charge-coupled device; FOV: Field of view; MIRACLE: Magnetometers Ionospheric Radars All-sky Cameras Large Experiment; EMCCD: Electron multiplying CCD; VFIT: Ion velocity fit; UHF: Ultrahigh frequency; IMAGE: International Monitor for Auroral Geomagnetic Effects; AU, AL: Auroral electrojet index; IU, IL: Auroral electrojet index from IMAGE magnetometers; LP: Langmuir probe; TII: Thermal ion imager; VFM: Vector field magnetometer; IMF: Interplanetary magnetic field; HSS: High-speed solar wind streams; SYM-H: Longitudinally symmetric disturbances of the geomagnetic H component; HWM: Horizontal

wind model; UT: Universal time; CHAOS-7: CHAMP, Ørsted, and SAC-C model of Earth's magnetic field.

Supplementary Information

The online version contains supplementary material available at <https://doi.org/10.1186/s40623-022-01710-6>.

Additional file 1. Measurements from successive Swarm passes over northern Europe. Swarm A measurements were analyzed to confirm the zonal component of the ion velocity at the trough minimum during previous and successive passes of the event over northern Europe. **Figure S1 a–c** show measurements along the previous pass from 17:05 to 17:10 UT on 2018 February 20. This pass was made approximately 90 min before the pseudo-breakup, which occurred at 18:35 UT. A trough minimum was located at 67.6–67.9°N, which is highlighted by a vertical bar in magenta. The SAPS or latitudinally extended westward plasma flow had not yet been well developed, but eastward plasma flows can be identified at the trough minimum along with westward flows. **d, e** show measurements from the successive pass from 20:12 to 20:17 UT. A trough minimum, highlighted by a magenta bar, was found at 68.6°N, and the eastward plasma flow was localized sharply at the trough minimum in the predominant westward flow.

Acknowledgements

The authors thank the institutes who maintain the IMAGE magnetometer array. Swarm is a European Space Agency Mission; EFI and VFM data analysis and operations are supported by European Space Agency and the Canadian Space Agency.

Author contributions

Author #1, SO, provided substantial contributions to the conception, design, and data analysis of the work. Author #2: HV was involved in interpretation of data and creation of new software used in the work. Authors #3, #4, #11, #12, #13, and #14, LC, AA, AS, KS, TTT, and TS, contributed to interpretation of data, respectively. Authors #5, #6, #7, #8, #9, and #10, MR, YO, TR, MK, KK, and BK, were involved in the acquisition and analysis of data, respectively. All authors read and approved the final manuscript.

Funding

This work has been supported by JSPS KAKENHI JP 16H06286, 21H04518, 21K18651, 21KK0059, 22H01283, and JPJSBP120194814. H. V. was partially supported by AF314664. This work was carried out by the joint research program of Planetary Plasma and Atmospheric Research Center, Tohoku University.

Availability of data and materials

All-sky camera images at Abisko, Kilpisjärvi, Longyearbyen, and Lovozero and the EISCAT Dynasonde data were obtained from individual PIs (Sodankylä Geophysical Observatory, Finland; Finnish Meteorological Institute, Finland; National Institute of Polar Research, Japan; and Polar Geophysical Institute, Russia; EISCAT Tromsø, Norway) after checking the quick-looks at their websites (space.fmi.fi/MIRACLE/ASC/, pc115.seg20.nipr.ac.jp/www/AQVN/index.html, pgi.ru/kagin/eng/, dynserv.eiscat.uit.no/). The Swarm data were obtained through their websites (swarm-diss.esa.int). The FPI quick-looks are available at www.soyama.org/data. Access and processing data of the solar wind and geomagnetic indices were obtained using SPEDAS V4.1 through spdf.gsfc.nasa.gov/pub/data/. Package of the CHAOS-7 model code was downloaded from <http://www.spacecenter.dk/files/magnetic-models/CHAOS-7>.

Declarations

Ethics approval and consent to participate

Not applicable.

Consent for publication

Not applicable.

Competing interests

There are no financial and non-financial competing interests for this work.

Author details

¹Institute for Space-Earth Environmental Research, Nagoya University, Nagoya, Japan. ²National Institute of Polar Research, Tachikawa, Japan. ³Space Physics and Astronomy Research Unit, University of Oulu, Oulu, Finland. ⁴European Incoherent Scatter Association, Tromsø, Norway. ⁵National Institute of Polar Research, Tachikawa, Japan. ⁶Sodankylä Geophysical Observatory, University of Oulu, Oulu, Finland. ⁷Finnish Meteorological Institute, Helsinki, Finland. ⁸Polar Geophysical Institute, Apatity, Russia. ⁹Department of Computer and Network Engineering, The University of Electro-Communications, Chofu, Japan. ¹⁰Graduate School of Science Planetary Plasma and Atmospheric Research Center, Tohoku University, Sendai, Japan.

Received: 29 March 2022 Accepted: 25 September 2022

Published online: 18 October 2022

References

- Aikio AT, Cai L, Nygrén T (2012) Statistical distribution of height-integrated energy exchange rates in the ionosphere. *J Geophys Res* 117:A10325. <https://doi.org/10.1029/2012JA018078>
- Anderson PC, Carpenter DL, Tsuruda K, Mukai T, Rich FJ (2001) Multisatellite observations of rapid subauroral ion drifts (SAID). *J Geophys Res* 106(A12):29585–29599. <https://doi.org/10.1029/2001JA000128>
- Baron MJ, Wand RH (1983) F region ion temperature enhancements resulting from Joule heating. *J Geophys Res* 88(A5):4114–4118. <https://doi.org/10.1029/JA088iA05p04114>
- Billett DD, Grocott A, Wild JA, Walach M-T, Kosch MJ (2018) Diurnal variations in global Joule heating morphology and magnitude due to neutral winds. *J Geophys Res Space Phys* 123:2398–2411. <https://doi.org/10.1002/2017JA025141>
- Billett DD, Hosokawa K, Grocott A, Wild JA, Aruliah AL, Ogawa Y et al (2020) Multi-instrument observations of ion-neutral coupling in the dayside cusp. *Geophys Res Lett*. <https://doi.org/10.1029/2019GL085590>
- Brekke A (2013) Physics of the upper polar atmosphere, Wiley Praxis Series in Atmospheric Physics. Springer, New York. <https://doi.org/10.1007/978-3-642-27401-5>
- Brekke A, Rino CL (1978) High-resolution altitude profiles of the auroral zone energy dissipation due to ionospheric currents. *J Geophys Res* 83(A6):2517–2524. <https://doi.org/10.1029/JA083iA06p02517>
- Cai L, Oyama S-I, Aikio A, Vanhamäki H, Virtanen I (2019) Fabry-Perot interferometer observations of thermospheric horizontal winds during magnetospheric substorms. *J Geophys Res Space Physics* 124:3709–3728. <https://doi.org/10.1029/2018JA026241>
- Conde M et al (2001) Assimilated observations of thermospheric winds, the aurora, and ionospheric currents over Alaska. *J Geophys Res* 106(A6):10493–10508. <https://doi.org/10.1029/2000JA000135>
- De Keyser J, Roth M, Lemaire J (1998) The magnetospheric driver of subauroral ion drifts. *Geophys Res Lett* 25:1625–1628. <https://doi.org/10.1029/98GL01135>
- Deng Y, Lu G, Kwak Y-S, Sutton E, Forbes J, Solomon S (2009) Reversed ionospheric convections during the November 2004 storm: Impact on the upper atmosphere. *J Geophys Res* 114:A07313. <https://doi.org/10.1029/2008JA013793>
- Dhadly M, Conde M (2017) Trajectories of thermospheric air parcels flowing over Alaska, reconstructed from ground-based wind measurements. *J Geophys Res Space Physics* 122:6635–6651. <https://doi.org/10.1002/2017JA024095>
- Dhadly MS, Emmert JT, Drob DP, Conde MG, Doornbos E, Shepherd GG, Makela JJ, Wu Q, Niciejewski RJ, Ridley AJ (2018) Seasonal dependence of geomagnetic active-time northern high-latitude upper thermospheric winds. *J Geophys Res Space Phys* 123:739–754. <https://doi.org/10.1002/2017JA024715>
- Erickson PJ et al (2016) Multipoint MMS observations of fine-scale SAPS structure in the inner magnetosphere. *Geophys Res Lett* 43:7294–7300. <https://doi.org/10.1002/2016GL069174>
- Finlay CC, Kloss C, Olsen N et al (2020) The CHAOS-7 geomagnetic field model and observed changes in the South Atlantic Anomaly. *Earth Planets Space* 72:156. <https://doi.org/10.1186/s40623-020-01252-9>
- Foster JC, Burke WJ (2002) SAPS: a new categorization for sub-auroral electric fields. *Eos Trans AGU* 83(36):393–394. <https://doi.org/10.1029/2002E0000289>
- Foster JC, Vo HB (2002) Average characteristics and activity dependence of the subauroral polarization stream. *J Geophys Res* 107(A12):1475. <https://doi.org/10.1029/2002JA009409>
- Fujii R, Nozawa S, Matuura N, Brekke A (1998) Study on neutral wind contribution to the electrodynamics in the polar ionosphere using EISCAT CP-1 data. *J Geophys Res* 103(A7):14731–14739. <https://doi.org/10.1029/97JA03687>
- Hedin AE et al (1996) Empirical wind model for the upper, middle and lower atmosphere. *J Atmos Terr Phys* 58:1421–1434. [https://doi.org/10.1016/0021-9169\(95\)00122-0](https://doi.org/10.1016/0021-9169(95)00122-0)
- Horvath I, Lovell BC (2017) Investigating the development of double-peak subauroral ion drift (DSAID). *J Geophys Res Space Physics* 122:4526–4542. <https://doi.org/10.1002/2016JA023506>
- Hosokawa K, Milan SE, Lester M, Kadokura A, Sato N, Björnsson G (2013) Large flow shears around auroral beads at substorm onset. *Geophys Res Lett* 40:4987–4991. <https://doi.org/10.1002/grl.50958>
- Imajo S, Miyoshi Y, Kazama Y et al (2021) Active auroral arc powered by accelerated electrons from very high altitudes. *Sci Rep* 11:1610. <https://doi.org/10.1038/s41598-020-79665-5>
- Kalafatoglou Eyigüler EC, Kaymaz Z, Frisell NA, Ruohoniemi JM, Rastätter L (2018) Investigating upper atmospheric Joule heating using cross-combination of data for two moderate substorm cases. *Space Weather* 16:987–1012. <https://doi.org/10.1029/2018SW001956>
- Kallio EI, Pulkkinen TI, Kiskinen HEJ, Viljanen A, Slavin JA, Ogilvie K (2000) Loading-unloading processes in the nightside ionosphere. *Geophys Res Lett*. <https://doi.org/10.1029/1999GL003694>
- Karlsson T, Marklund GT, Blomberg LG, Mälkki A (1998) Subauroral electric fields observed by the Freja satellite: a statistical study. *J Geophys Res* 103(A3):4327–4341. <https://doi.org/10.1029/97JA00333>
- Kataoka R, Hosokawa K, Nishitani N, Miyoshi Y (2009) SuperDARN Hokkaido radar observation of westward flow enhancement in subauroral latitudes. *Ann Geophys* 27(4):1695–1699
- Kauristie K, Pulkkinen TI, Pellinen RJ, Opgenoorth HJ (1996) What can we tell about global auroral-electrojet activity from a single meridional magnetometer chain? *Ann Geophys* 14:1177–1185. <https://doi.org/10.1007/s00585-996-1177-1>
- Kiene A, Bristow WA, Conde MG, Hampton DL (2018) Measurements of ion-neutral coupling in the auroral F region in response to increases in particle precipitation. *J Geophys Res Space Physics* 123:3900–3918. <https://doi.org/10.1002/2017JA024999>
- Kiene A, Bristow WA, Conde MG, Hampton DL (2019) High-resolution local measurements of F region ion temperatures and Joule heating rates using SuperDARN and ground-based optics. *J Geophys Res Space Physics* 124:557–572. <https://doi.org/10.1029/2018JA025997>
- Killeen TL, Hays PB, Carignan GR, Heelis RA, Hanson WB, Spencer NW, Brace LH (1984) Ion-neutral coupling in the high-latitude F region: evaluation of ion heating terms from Dynamics Explorer 2. *J Geophys Res* 89(A9):7495–7508. <https://doi.org/10.1029/JA089iA09p07495>
- Knudsen DJ, Burchill JK, Buchert SC, Eriksson AI, Gill R, Wahlund J-E, Åhlen L, Smith M, Moffat B (2017) Thermal ion imagers and Langmuir probes in the Swarm electric field instruments. *J Geophys Res Space Physics*. <https://doi.org/10.1002/2016JA022571>
- Koustov A, Nishitani N, Ebihara Y, Kikuchi T, Hairston MR, Andre D (2008) Subauroral polarization streams: observations with the Hokkaido and King Salmon SuperDARN radars and modeling. *Ann Geophys* 26:3317–3327
- Kozelov BV, Pilgaev SV, Borovkov LP, Yurov VE (2012) Multi-scale auroral observations in Apatity: winter 2010–2011. *Geosci Instrum Method Data Syst* 1:1–6. <https://doi.org/10.5194/gi-1-1-2012>
- Larsen MF (2002) Winds and shears in the mesosphere and lower thermosphere: results from four decades of chemical release wind measurements. *J Geophys Res*. <https://doi.org/10.1029/2001JA000218>
- Lomidze L, Knudsen DJ, Burchill J, Kouznetsov A, Buchert SC (2018) Calibration and validation of Swarm plasma densities and electron temperatures using ground-based radars and satellite radio occultation measurements. *Radio Sci* 53:15–36. <https://doi.org/10.1002/2017RS006415>
- Lu G, Richmond AD, Emery BA, Roble RG (1995) Magnetosphere-ionosphere-thermosphere coupling: Effect of neutral winds on energy transfer and

- field-aligned current. *J Geophys Res* 100(A10):19643–19659. <https://doi.org/10.1029/95JA00766>
- Makarevich RA, Bristow WA (2014) Fine structure of subauroral electric field and electron content. *J Geophys Res Space Physics* 119:3789–3802. <https://doi.org/10.1002/2014JA019821>
- Maynard NC (1978) On large poleward-directed electric fields at sub-auroral latitudes. *Geophys Res Lett* 5:617–618. <https://doi.org/10.1029/GL005i007p00617>
- Mishin EV, Burke WJ, Huang CY, Rich FJ (2003) Electromagnetic wave structures within subauroral polarization streams. *J Geophys Res* 108(A8):1309. <https://doi.org/10.1029/2002JA009793>
- Nagano H, Nishitani N, Hori T (2015) Occurrence characteristics and lowest speed limit of subauroral polarization stream (SAPS) observed by the SuperDARN Hokkaido East radar. *Earth Planet Sp* 67:126. <https://doi.org/10.1186/s40623-015-0299-7>
- Ogawa Y, Tanaka Y, Kadokura A, Hosokawa K, Ebihara Y, Motoba T, Gustavsson B, Brändström U, Sato Y, Oyama S, Ozaki M, Raita T, Sigernes F, Nozawa S, Shiokawa K, Kosch M, Kauristie K, Hall C, Suzuki S, Miyoshi Y, Gerrard A, Miyaoka H, Fujii R (2020) Development of low-cost multi-wavelength imager system for studies of aurora and airglow. *Polar Sci* 23:100501. <https://doi.org/10.1016/j.polar.2019.100501>
- Oyama S et al (2009) Spatial evolution of frictional heating and the predicted thermospheric wind effects in the vicinity of an auroral arc measured with the Sondrestrom incoherent-scatter radar and the Reimei satellite. *J Geophys Res* 114:A07311. <https://doi.org/10.1029/2009JA014091>
- Oyama S, Shinbori A, Ogawa Y, Kellinsalmi M, Raita T, Aikio A et al (2020) An ephemeral red arc appeared at 68° MLat at a pseudo breakup during geomagnetically quiet conditions. *J Geophys Res Space Phys*. <https://doi.org/10.1029/2020JA028468>
- Pfaff R (2012) The near-earth plasma environment. *Space Sci Rev* 168:23–112. <https://doi.org/10.1007/s11214-012-9872-6>
- Rich FJ, Burke WJ, Kelley MC, Smiddy M (1980) Observations of field-aligned currents in association with strong convection electric fields at subauroral latitudes. *J Geophys Res* 85(A5):2335–2340. <https://doi.org/10.1029/JA085iA05p02335>
- Richmond AD (1995) The ionospheric wind dynamo: effects of its coupling with different atmospheric regions. In: Johnson RM, Killeen TL (eds) *The Upper Mesosphere and Lower Thermosphere*. American Geophysical Union, Washington, pp 49–65
- Richmond AD, Lathuillière C, Vennerstroem S (2003) Winds in the high-latitude lower thermosphere: Dependence on the interplanetary magnetic field. *J Geophys Res* 108:1066. <https://doi.org/10.1029/2002JA009493>
- Richmond AD, Thayer JP (2000). Ionospheric Electrodynamics: A Tutorial. In: S.-I. Ohtani, R. Fujii, M. Hesse and R.L. Lysak, *Magnetospheric Current Systems*. <https://doi.org/10.1029/GM118p0131>
- Ritter P, Lühr H, Rauberg J (2013) Determining field-aligned currents with the Swarm constellation mission. *Earth Planet Sp* 65:9. <https://doi.org/10.5047/eps.2013.09.006>
- Rodríguez-Zuluaga J, Stolle C, Park J (2017) On the direction of the Poynting flux associated with equatorial plasma depletions as derived from Swarm. *Geophys Res Lett*. <https://doi.org/10.1002/2017gl073385>
- Sakaguchi K, Shiokawa K, Ieda A, Nomura R, Nakajima A, Greffen M, Donovan E, Mann IR, Kim H, Lessard M (2009) Fine structures and dynamics in auroral initial brightening at substorm onsets. *Ann Geophys* 27:623–630
- Sakanai T, Fukunishi H, Okano S, Sato N, Yamagishi H, Yukimatu AS (2002) Dynamical coupling of neutrals and ions in the high-latitude F region: simultaneous FPI and HF radar observations at Syowa station, Antarctica. *J Geophys Res* 107(A11):1388. <https://doi.org/10.1029/2001JA007530>
- Sangalli NL, Partamies M, Syrjäsoo CF, Enell K, Kauristie S, Mäkinen (2011) Performance study of the new EMCCD-based all-sky cameras for auroral imaging. *Int J Remote Sensing* 32(11):2987–3003.5. <https://doi.org/10.1080/01431161.2010.541505>
- Sedgemore KJF, Williams PJS, Jones GOL, Wright JW (1996) A comparison of EISCAT and Dynasonde measurements of the auroral ionosphere. *Ann Geophys* 14:1403–1412. <https://doi.org/10.1007/s00585-996-1403-x>
- Sedgemore KJF, Wright JW, Williams PJS, Jones GOL, Rietveld MT (1998) Plasma drift estimates from the Dynasonde: comparison with EISCAT measurements. *Ann Geophys* 16:1138–1143. <https://doi.org/10.1007/s00585-998-1138-y>
- Shiokawa K, Kadota T, Otsuka Y, Ogawa T, Nakamura T, Fukao S (2003) A two-channel Fabry-Perot interferometer with thermoelectric-cooled CCD detectors for neutral wind measurement in the upper atmosphere. *Earth Planets Space* 55(5):271–275. <https://doi.org/10.1186/BF03351759>
- Shiokawa K, Otsuka Y, Oyama S et al (2012) Development of low-cost sky-scanning Fabry-Perot interferometers for airglow and auroral studies. *Earth Planet Sp* 64:1033–1046. <https://doi.org/10.5047/eps.2012.05.004>
- Smiddy M, Kelley MC, Burke W, Rich F, Sagalyn R, Shuman B, Hays R, Lai S (1977) Intense poleward-directed electric fields near the ionospheric projection of the plasmopause. *Geophys Res Lett* 4:543–546. <https://doi.org/10.1029/GL004i011p00543>
- Southwood DJ, Wolf RA (1978) An assessment of the role of precipitation in magnetospheric convection. *J Geophys Res* 83(A11):5227–5232. <https://doi.org/10.1029/JA083iA11p05227>
- Spiro RW, Heelis RA, Hanson WB (1979) Rapid subauroral ion drifts observed by Atmosphere Explorer C. *Geophys Res Lett* 6:657–660. <https://doi.org/10.1029/GL006i008p00657>
- Streltsov AV, Mishin EV (2003) Numerical modeling of localized electro-magnetic waves in the nightside subauroral zone. *J Geophys Res* 108(A8):1332. <https://doi.org/10.1029/2003JA009858>
- Tanskanen EI, Viljanen A, Pulkkinen TI, Pirjola R, Häkkinen L, Pulkkinen A, Amm O (2001) At substorm onset, 40% of AL comes from underground. *J Geophys Res* 106(A7):13119–13134. <https://doi.org/10.1029/2000JA001135>
- Thayer JP (1998) Height-resolved Joule heating rates in the high-latitude E region and the influence of neutral winds. *J Geophys Res* 103(A1):471–487. <https://doi.org/10.1029/97JA02536>
- Thayer JP, Vickrey JF, Heelis RA, Gary JB (1995) Interpretation and modeling of the high-latitude electromagnetic energy flux. *J Geophys Res* 100(A10):19715–19728. <https://doi.org/10.1029/95JA01159>
- Vanhamäki H, Yoshikawa A, Amm O, Fujii R (2012) Ionospheric Joule heating and Poynting flux in quasi-static approximation. *J Geophys Res* 117:A08327. <https://doi.org/10.1029/2012JA017841>
- Wang H, Lühr H, Häusler K, Ritter P (2011) Effect of subauroral polarization streams on the thermosphere: a statistical study. *J Geophys Res* 116:A03312. <https://doi.org/10.1029/2010JA016236>
- Wang H, Lühr H, Ma SY (2012a) The relation between subauroral polarization streams, westward ion fluxes, and zonal wind: seasonal and hemispheric variations. *J Geophys Res* 117:A04323. <https://doi.org/10.1029/2011JA017378>
- Wang H, Lühr H, Ritter P, Kervalishvili G (2012b) Temporal and spatial effects of subauroral polarization streams on the thermospheric dynamics. *J Geophys Res* 117:A11307. <https://doi.org/10.1029/2012JA018067>
- Wright JW, Pitteway MLV (1994) High-resolution vector velocity determinations from the dynasonde. *J Atmos Terr Phys* 56(8):961–977. [https://doi.org/10.1016/0021-9169\(94\)90157-0](https://doi.org/10.1016/0021-9169(94)90157-0)
- Xiong C, Lühr H, Fejer BG (2015) Global features of the disturbance winds during storm time deduced from CHAMP observations. *J Geophys Res Space Physics* 120:5137–5150. <https://doi.org/10.1002/2015JA021302>

Publisher's Note

Springer Nature remains neutral with regard to jurisdictional claims in published maps and institutional affiliations.

Submit your manuscript to a SpringerOpen[®] journal and benefit from:

- Convenient online submission
- Rigorous peer review
- Open access: articles freely available online
- High visibility within the field
- Retaining the copyright to your article

Submit your next manuscript at ► [springeropen.com](https://www.springeropen.com)